

X-RAYING THE CORONAE OF HD 155555

S. LALITHA¹, K.P. SINGH¹, S.A. DRAKE², & V. KASHYAP³

1. Tata Institute of Fundamental Research, Homi Bhabha road, Mumbai 400005, India

2. NASA Goddard Space Flight Center, Code 662, Greenbelt, MD 20771, USA

3. Harvard-Smithsonian Center for Astrophysics, 60 Garden St., Cambridge, 02138, MA, USA

The Astrophysical Journal

ABSTRACT

We present an analysis of the high-resolution *Chandra* observation of the multiple system, HD 155555 (an RS CVn type binary system, HD 155555 AB, and its spatially resolved low-mass companion HD 155555 C). This is an intriguing system which shows properties of both an active pre-main sequence star and a synchronised (main sequence) binary. We obtain the emission measure distribution, temperature structures, plasma densities, and abundances of this system and compare them with the coronal properties of other young/active stars. HD 155555 AB and HD 155555 C produce copious X-ray emission with $\log L_x$ of 30.54 and 29.30, respectively, in the 0.3-6.0 keV energy band. The light curves of individual stars show variability on timescales of few minutes to hours. We analyse the dispersed spectra and reconstruct the emission measure distribution using spectral line analysis. The resulting elemental abundances exhibit inverse first ionisation potential effect in both cases. An analysis of He-like triplets yields a range of coronal electron densities $\sim 10^{10} - 10^{13} \text{ cm}^{-3}$. Since HD 155555 AB is classified both as an RS CVn and a PMS star, we compare our results with those of other slightly older active main-sequence stars and T Tauri stars, which indicates that the coronal properties of HD 155555 AB closely resemble that of an older RS CVn binary rather than a younger PMS star. Our results also suggests that the properties of HD 155555 C is very similar to those of other active M dwarfs.

Subject headings: stars: activity, stars: coronae, stars: low-mass, pre-main sequence, stars: individual: HD 155555, techniques:spectroscopic, X-ray:stars

1. INTRODUCTION

RS Canum Venaticorum (RS CVn) type stellar systems are close binaries containing late type evolved G/K stars (Hall 1980). Typical orbital periods of these systems range from less than a day to a few months and, with a few exceptions such as λ And, the rotation periods of the close components are spun up to match their orbital period due to the tidal synchronization forces. As a result of their rapid rotation and deep convective envelopes, RS CVns have powerful magnetic dynamos which generate enormous amounts of magnetic flux which, emerging into their outer layers, produces enhanced stellar activity. For example, RS CVns show optical variability due to the rotational modulation of an asymmetrical distribution of cool spots which can cover $> 10\%$ of their surfaces. Studies of RS CVns in chromospheric lines such as Ca II H and K and H-alpha and in the ultraviolet and X-ray bands show that an enormous amount of energy (compared to stars like the Sun) is being released into their chromospheres and coronae, in both their typical (sometimes, called quiescent) and flaring states. Their intense X-ray activity was first detected by the HEAO-1 observatory (Walter & Bowyer 1981) and has been extensively studied since by subsequent missions such as *Einstein*, *EXOSAT*, *ROSAT*, *ASCA*, *Chandra* and *XMM-Newton*. The X-ray luminosities of RS CVn binaries are typically in the range of $30 < \log L_x < 32$ (ergs s⁻¹), corresponding to 10^{-4} to 10^{-3} of their bolometric luminosities, and $\log L_x$ values > 33 have been observed in large RS CVn flares (e.g. the Swift-detected flare of SZ Psc discussed by Drake et al. 2015).

Pre-main-sequence and early (zero-age) main-sequence

solar- and sub-solar-mass stars have retained much of the angular momentum of their original protostellar predecessors, and thus have rotation rates from less than a day to ~ 10 days, much in excess of the present solar rotation rate. As a result, just like active synchronized binaries with similar rotation rates, young stars have powerful chromospheres and coronae. As they evolve, their rotation rates, and consequently their activity levels, drop due to the loss of angular momentum in stellar winds. The coronae of very young (ages $< 5 - 10$ Myr) stars have been well-studied due to their locations in large nearby stellar associations and clusters, such as Tau-Aur and Orion OB1. Young, late-type pre-main sequence stars are luminous X-ray sources. This is indeed observed in T Tauri stars which are divided into two classes the Classic T Tauri stars (CTTS) and weak-line T Tauri stars (WTTS). The CTTS shows a strong H α emission lines and infra-red excess as a result of the accretion, whereas, WTTS display weak H α line and no infrared excess. Güdel et al. (2007) surveyed the Taurus molecular cloud and found evidence for lower X-ray luminosities in CTTS compared to WTTS. However, the X-ray emission of a fraction of CTTS, exhibits an additional soft, high-density component that has been attributed to a magnetically confined accretion column, e.g., the 8-Myr old TW Hya (Kastner et al. 2002). It has only been in the last 3 decades that the existence of a population of somewhat older (10 - 300 Myr) stars permeating the solar neighborhood in kinematically homogeneous stellar moving groups has been recognized, e.g., AB Dor (Rucinski 1982), Speedy Mic (Bromage et al. 1992), etc. A few pre-main sequence stars also show evidence of soft extended

X-ray emission close to the star that is thought to arise in accretion-related jet-like outflows, for example, DG Tau (Güdel et al. 2005), Z CMa (Stelzer et al. 2009), RY Tau (Skinner et al. 2011).

There has been some discussion in the literature as to whether the details of coronal and chromospheric activity in cool stars differs due to the underlying origin of their rapid rotation, i.e., spin-up in close binary systems vs. youth, but few definitive conclusions have been reached. A number of flares in active binaries observed in the radio have been observed by VLBI to have an extent similar to the separation between the two components (e.g., Little-Marenin et al. 1986, suggesting that they may be related to inter-binary magnetic reconnection, but X-ray observations lack the milli-arcsecond spatial resolution needed for this type of analysis). There have been some indirect tests: e.g., Singh et al. (1996), compared 59 RS CVn binaries containing 2 late-type components to 29 Algol-type binaries most of which had only one late-type component, and found a tendency for RS CVns to be 3-4 times more X-ray luminous than Algols with the same orbital period, suggesting that there may be additional energy release in their coronae due to interconnecting magnetic field reconnections and/or disconnections. The most significant difference in the coronal properties of active RS CVns like AR Lac or active (pre-main sequence) binary system HD 98000 and active accreting (pre-main sequence) single stars like TW Hya are due to the presence of an accretion-related soft ($T \sim 2 - 4$ MK) plasma component in CTTS; there can also be additional variability in the X-ray emission of CTTS due to varying absorption by circumstellar material and/or fluctuations in the accretion rate, e.g., Flaccomio et al. (2010).

The intense coronal X-ray activity in the low mass RS CVn type binaries is a key characteristic in investigating the properties and evolution of low mass late-type stellar objects, spurring extensive studies with several X-ray satellites over the last few decades (Audard et al. 2003). The Sun is usually considered a prototype of low mass cool stars, hence we often extrapolate the knowledge we have on the Sun to the other stars. The X-ray emission and the temperature of the coronal plasma of such stars are, however, at least a magnitude higher than the solar coronal emission indicating a fundamental difference in the dynamo powering the coronal activity. Most of the earlier studies, with a few exceptions, have been performed using low spectral resolution instruments, which were not able to provide very reliable information on coronal plasma. The unprecedented spectral resolution provided by X-ray gratings and large effective area of X-ray telescopes like *Chandra* X-ray observatory and *XMM-Newton*, allows us to resolve individual lines thus providing plasma diagnostics of coronae of stars other than the Sun. In particular, an updated picture of coronal abundance anomalies based on observations of HR 1099 confirmed its depletion in the abundance of low first ionisation potential (FIP) elements in comparison to the high-FIP elements (Brinkman et al. 2001; Drake & Kashyap 2001; Güdel et al. 2001). Later, Audard et al. (2002) showed that stars with different activity level show a continuum of behaviour from the FIP effect to the inverse FIP (iFIP) effect.

Spectral diagnostics based on a large number of prominent emission lines can be used to derive the temper-

atures, density structure of emitting plasma, emission processes and ionisation properties of the coronal X-ray plasma. Furthermore, based on the electron density and coronal temperatures we can infer the pressure and the volume of the emitting plasma. Since stellar coronal structures are spatially unresolved, unlike the solar coronal loops, by combining all the above results one can also derive useful information about the coronal loop properties (Reale et al. 1997; Güdel & Nazé 2009; Fuhrmeister et al. 2011).

Finally, we can compare the high-resolution X-ray spectroscopic data with that of other low mass stars with different ages which are crucial for understanding how the stellar activity and coronal properties change during these different evolutionary phases (Ball et al. 2005; Robrade & Schmitt 2005).

Here, we report the first high spectral resolution observations of the HD 155555 system with *Chandra* HETG with the objective of getting a better insight into the hottest part of the outer stellar atmosphere of the active stars in HD 155555 system. Although stellar activity has been observed and studied for decades, the exact mechanism controlling the magnetic activity in low-mass stars are still not understood. The fundamental parameters must be derived for a range of stars in order to provide the basis for a theoretical understanding. Our goal is to use the X-ray light curves and spectra of an active RS CVn system to address several issues: monitor the flares, determine the emission measure and temperature distribution, determine abundances, probe the density diagnostics and compare to other stars in different evolutionary states. This paper is organised as follows: in § 2 we discuss the properties of HD 155555 system; § 3 presents the details of the X-ray observation and the methods adopted for the data analysis; in § 4 we describe the procedures used to obtain the emission measures, the abundances and the electron densities of HD 155555 AB. In § 5, we analyse the time variability and spectral properties of HD 155555 C. We discuss the implications of the analyses of both HD 155555 AB and the companion HD 155555 C in § 6 and summarise our conclusions in § 7.

2. THE HD 155555 SYSTEM

HD 155555 (V824 Ara), is a young (≈ 18 Myr, Strassmeier & Rice 2000) RS CVn binary which also shows some characteristics common to the pre-main sequence stars. It is a triple star system consisting of cool stars: G5IV, a K0IV and an M3V star. Two of the three stars (G and K stars) are in a close binary system with an orbital period of 1.68d (Strassmeier & Rice 2000) and will together be referred to as HD 155555 AB, henceforth. The M dwarf companion LDS 536 B is $33''$ away from the primary close-in binary system, and henceforth will be referred to as HD 155555 C. Pasquini et al. (1991) suggested that HD 155555 AB and HD 155555 C are part of a young disk which is in agreement with the high lithium abundance in both the components. Later, based on the Hipparcos satellite the distance to the HD 155555 system has been determined to be 31 pc (Strassmeier & Rice 2000). The properties of the stars in HD 155555 system are summarised in Table 1.

HD 155555 AB exhibits all the characteristics nominally attributed to the RS CVn class of stars, viz., strong

Ca II H and K emission due to chromospheric activity and photometric variability as a result of spot migration (Cutispoto 1990). Dunstone et al. (2008) have shown that both the components of the HD 155555 system are particularly interesting because it is an unusual RS CVn in which the close-in binaries have become synchronised rotators as they evolved towards the main sequence; most RS CVn systems synchronise much later in their lifetimes as one/both stars evolve away from the main sequence. Thus, without the binarity factor, HD 155555 system would still be active, since they are rapidly rotating cool stars. The binarity of this system has, however, set the orbital period to 1.68d which is shorter than if this were a single star. It is likely that while both age and binarity have worked together to produce activity, in this case, the latter has determined the exact period.

TABLE 1
PHYSICAL PARAMETERS OF THE HD 155555 SYSTEM.

Parameter	HD 155555A	HD 155555B	HD 155555 C
V_{mag}	6.72		12.82
T [K]	5500 ± 100	5050 ± 150	3300 ± 150
Spectral type	G5IV	K0IV	M3V
P [days]	1.68	1.68	
Inclination i	$52.5^0 \pm 2.5$	$52.5^0 \pm 2.5$	$50^0 \pm 5$
$V \sin i$ [km s $^{-1}$]	36.8 ± 1.0	33.7 ± 1.5	≤ 3
$R \sin i$ [R_{\odot}]	1.55 ± 0.18	1.21 ± 0.25	
$M \sin i$ [M_{\odot}]	1.10 ± 0.01	1.00 ± 0.01	
$\log L_{bol}$ [erg s $^{-1}$]	33.89		32.26

References. (a) Pasquini et al. (1989); (b) Strassmeier & Rice (2000).

The stars in HD 155555 AB probably exhibit substantial differential rotation which is a key factor in the generation of stellar magnetic fields. A very high level of activity has also been reported from the visual companion HD 155555 C (Martin & Brandner 1995). The X-ray emission from HD 155555 AB was first reported by *HEAO-1* A2 low energy experiment (Walter et al. 1980). It was found to be a relatively strong X-ray source with $\log L_x \approx 1.0 \times 10^{31}$ erg s $^{-1}$, yielding a $\log \frac{L_x}{L_{bol}} \sim -2.9$ in 0.5-3 keV energy range, making it a very active binary system. It was subsequently observed by several other X-ray satellites and a summary of observed X-ray fluxes and the corresponding luminosities is given in Table 2. The low X-ray flux observed by *EXOSAT* LE could be due to poor calibration. HD 155555 C was discovered serendipitously during *EXOSAT* observations of HD 155555 AB (Pasquini et al. 1989). The X-ray luminosity of HD 155555 C was found to be $\sim 3 \times 10^{29}$ erg s $^{-1}$ in 0.04-2.0 keV energy band, yielding a $\log \frac{L_x}{L_{bol}} \sim -2.8$, suggesting that HD 155555 C is also a very active young star.

3. THE CHANDRA DATA

The HD 155555 system was observed for ~ 94 ks starting on 2002 July 10 11:27 UT, using the HETG (Weisskopf et al. 2002) and Advanced Camera for Imaging Spectroscopy (ACIS, Garmire et al. 2003) on-board *Chandra* X-ray observatory (ObsID 2538). The data obtained from the public *Chandra* Data Archives were reprocessed following the *Chandra* Interactive Analysis

TABLE 2
THE X-RAY LUMINOSITY OF THE HD 155555 AB SYSTEM.

Instruments	Unabsorbed F_X 10 $^{-11}$ erg s $^{-1}$ cm $^{-2}$	L_x 10 30 erg s $^{-1}$	Ref.
<i>HEAO-1</i> A2 (0.5-3.0 keV)	9.0	10.31	(a)
<i>EXOSAT</i> (0.04-2.0 keV)	0.9-1.1	1.03-1.26	(b)
<i>ROSAT</i> PSPC (0.1-2.4 keV)	3.8	4.35	(c)
<i>ROSAT</i> HRI (0.1-2.4 keV)	3.7-4.6	4.23-5.26	(c)
<i>XMM-Newton</i> (0.2-12.0 keV)	5.7	6.52	(d)
<i>Chandra</i> HETG (0.3-6.0 keV)	2.8-3.6	3.20-4.12	(e)
	2.4-3.0	2.74-3.43	(e)

References. (a) Walter et al. (1980); (b) Barstow (1987); (c) Using XSPEC v13.0 and WebPIMMS v4.7 and assuming a coronal temperature of 10 MK, we estimated $ECF_{PSPC} = 7.9 \times 10^{-12}$ erg s $^{-1}$ cm $^{-2}$ and $ECF_{HRI} = 2.5 \times 10^{-11}$ erg s $^{-1}$ cm $^{-2}$; (d) observed during XMM-Newton slew survey and converted to flux using the flux limit 1.3×10^{-11} erg s $^{-1}$ cm $^{-2}$; (e) present work.

of Observations (CIAO ver 4.5)¹ science threads, and XSPEC V13.0 (Arnaud 1996) was used for spectral analysis.

To optimize the signal-to-noise ratio in the spectrum, CIAO includes position-dependent PHA filtering of the data. We used the TGEXTRACT tool available in the CIAO to extract the -1 and +1 grating orders of HEG and MEG, and used the *add_grating_orders* script to sum the orders to improve the counts statistics. We used the default binning of 0.005Å for MEG and 0.0025Å for HEG. The background spectrum was extracted from source-free symmetrical regions near the source region, with each region having an area of the order of few times that of the source area. We computed the net spectrum of HD 155555 AB and HD 155555 C by subtracting the background spectrum. The spectra were then scaled to the area of the source region, to get the source spectrum for both +1 and -1 orders. The positive and negative orders spectra for each of the sources were then combined to get the final spectrum. The co-added negative and positive first order MEG and HEG spectrum of HD 155555 AB and HD 155555 C for the entire observation are shown in Figure 1 and 2. There are numerous well resolved lines with high signal-to-noise ratio present in the spectrum and these have been labelled in the figures.

Furthermore, we re-ran the CIAO data reduction pipeline and extracted the zeroth-order spectrum of both HD 155555 AB and HD 155555 C. The zeroth-order spectrum is a low-resolution spectrum created by the photons that pass through the grating without being diffracted. The net count rate for HD 155555 AB and HD 155555 C zeroth order spectrum is $0.23 \pm 1.58 \times 10^{-3}$ and $3.96 \times 10^{-2} \pm 6.54 \times 10^{-4}$ counts s $^{-1}$, respectively. Based on the observation of HD 155555 system, PIMMS predicts a large pile-up fraction of $>20\%$; hence, we chose to use only the dispersed spectrum for our analysis.

4. ANALYSIS AND RESULTS: HD 155555 AB

¹ see <http://cxc.harvard.edu/ciao/threads/>

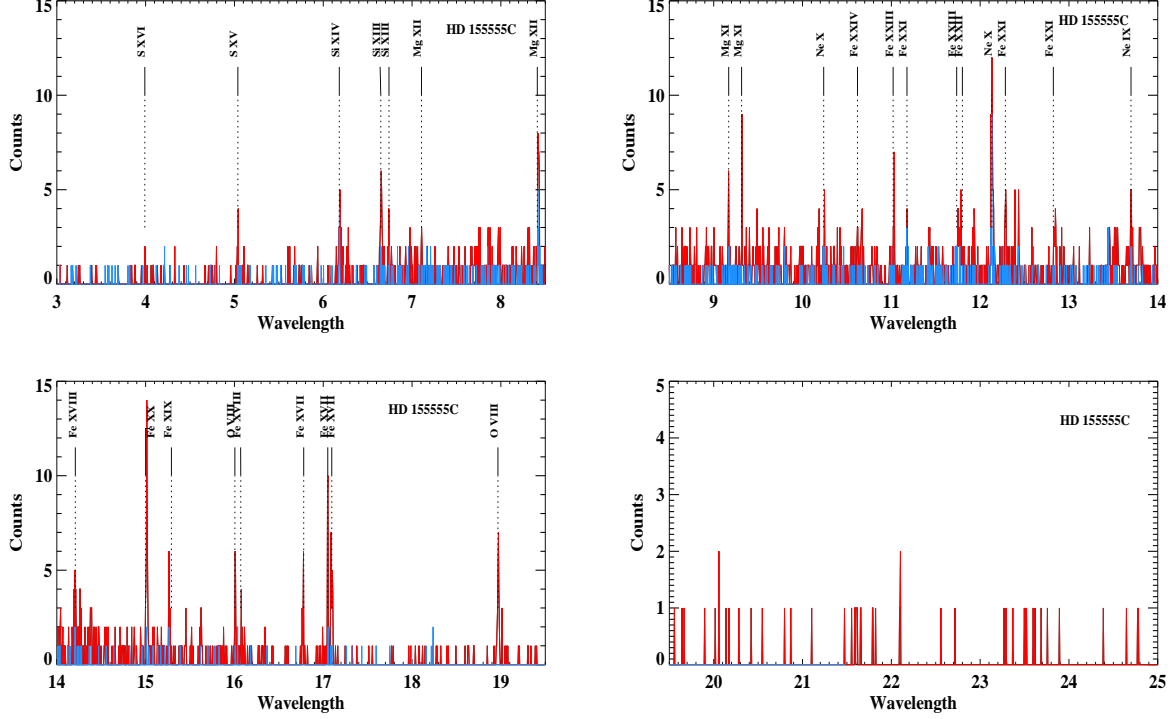


FIG. 2.— Combined \pm order spectrum of HD 155555 C for the entire observation binned to 0.005\AA for MEG (red) and 0.0025\AA for HEG (blue). The prominent lines are labeled.

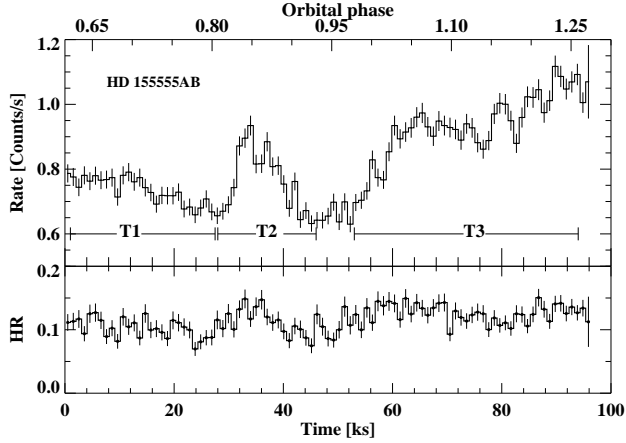


FIG. 3.— Top panel: Background subtracted X-ray light curve in 0.4-6.0 keV energy band and the corresponding orbital phase assuming an orbital period of ~ 1.68 days for HD 155555 AB. Bottom panel: The time variability of the ratio of number of counts in the 2.0-6.0 keV band to the number of counts in the 0.4-2.0 keV band for HD 155555 AB.

at 18.97\AA but they show very marginal variation or no significant variation. The detection of a dip in Ne X seen close to $\phi \sim 1.0$ and coinciding with the dip in the total intensity in Fig. 3 could indicate that moderately cool gas gives rise to this feature. The rise in the Ne X flux towards the end of the observation probably indicates the presence of a large active region on the surface of the star moving into the line of sight.

4.2. Spectroscopic behaviour

We divided the source spectra into three time-intervals as mentioned above and carried out a detailed spectral

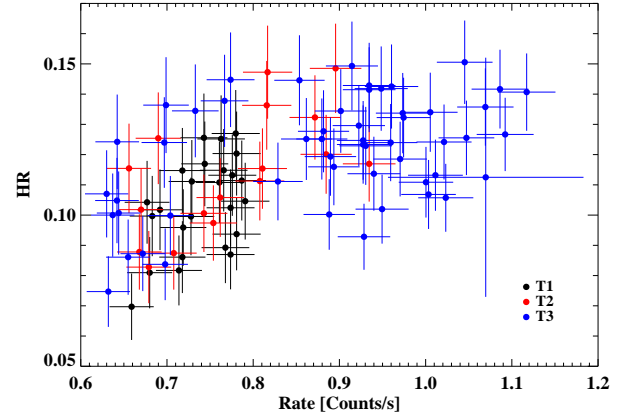


FIG. 4.— Hardness ratio of HD 155555 AB as function of the background subtracted X-ray count rate in 0.4-6.0 keV energy band. The black, red and blue filled circles refer to the T1, T2 and T3, respectively, (see text for details).

analysis for each of these intervals to investigate the temperature, the emission measure, the abundance and the density variation of the coronal plasma in HD 155555 AB. The analysis was carried out by global fitting using XSPEC as well as line by analysis of prominent lines using PINTofALE.

4.2.1. XSPEC fitting

We have characterised the thermal structure and the elemental abundance composition of the coronae of HD 155555 AB using the simultaneous global fitting to the HEG and MEG spectra. The temperatures and abundances relative to the solar values

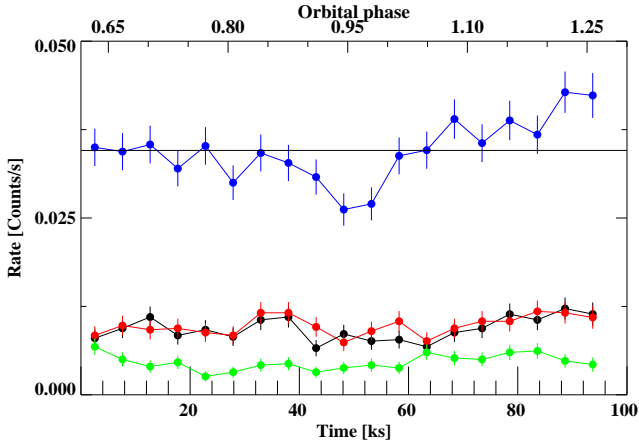


FIG. 5.— X-ray light curve from combined MEG +1 and -1 order counts for HD 155555 AB in the Mg XI at 8.41 Å (green), Ne X at 12.13 Å (blue), Fe XVII at 15.01 Å (red) and O VIII at 18.97 Å (black). The mean count rate for Ne X line is indicated by a thick vertical black line.

(Grevesse & Sauval 1998) were determined by simultaneous iterative XSPEC fit to the HEG and MEG spectra with Variable Astrophysical Emission Code (VAPEC) for thermal optically thin plasma models (Smith et al. 2001). We determined the number of VAPEC components with different temperatures by adding a new component until the addition of the next component did not improve the fit. Assuming that the corona of a star is not isothermal and has multi-temperature components, we used two-temperature VAPEC models. This produced a $\chi^2_{min} \sim 611$ (DOF ~ 711), $\chi^2_{min} \sim 412$ (DOF ~ 591), and $\chi^2_{min} \sim 1419$ (DOF ~ 1320) for time bins T1, T2 and T3, respectively, showing that 2T VAPEC models are a good fit to the data. We then added a new temperature component which reduced the minimum χ^2 further to $\chi^2_{min} \sim 520$ (DOF ~ 709), $\chi^2_{min} \sim 368$ (DOF ~ 589), and $\chi^2_{min} \sim 1245$ (DOF ~ 1318) for time bins T1, T2 and T3, respectively. The F-test produces a p-value of 0.017, 0.0913 and 0.0096 for time bins T1, T2 and T3, respectively. These p-values could under-state the evidence for the extra component by factors of 2 (Protassov et al. 2002), so we use a 3T model. Adding a 4th temperature component yields an F-test p-values 0.48, 0.47 and 0.50 for time bins T1, T2 and T3, respectively, which are unambiguously large. Hence, we use the 3T VAPEC models to describe of the dispersed spectra of HD 155555 AB. We allowed the abundance of all the elements to vary freely for each of the time bins. However, we fixed them to the same abundance values for each of the temperature components in the 3T VAPEC. For example, in the case of time bin T1 we allowed the O, Ne, Mg, Al, Si, S, Ar, Fe and Ni abundances vary freely while tying all the temperature components to the same abundance value for a given element. We, thus obtain a unique solution for the abundances for each time bin separately and also the temperatures, and emission measures. The best-fit temperatures and the emission measures for time intervals T1, T2 and T3 are presented in Table 4, whereas the best-fit abundance values are listed in Table 5. The unabsorbed X-ray flux of HD 155555 AB in 0.3-6.0 keV energy band is in the range $\sim 2.8 - 3.6 \times 10^{-11}$ erg s $^{-1}$ cm $^{-2}$, implying $L_X = 3.20-4.12 \times 10^{30}$ erg s $^{-1}$.

TABLE 4
BEST-FIT SPECTRAL PARAMETERS OBTAINED FOR TIME INTERVALS T1, T2, T3 FROM ITERATIVE FITTING OF DISPERSED X-RAY SPECTRA FOR HD 155555 AB DATA USING 3T VAPEC PLASMA MODELS. SEE TABLE 5 FOR THE BEST-FIT ELEMENTAL ABUNDANCES.

Parameters	T1	T2	T3
log t_1 [K]	6.72 ± 0.03	6.74 ± 0.07	6.64 ± 0.05
EM $_1$ [cm $^{-3}$]	$52.92^{+0.10}_{-0.11}$	$52.94^{+0.12}_{-0.24}$	$52.93^{+0.02}_{-0.19}$
log t_2 [K]	7.03 ± 0.05	7.01 ± 0.07	6.94 ± 0.02
EM $_2$ [cm $^{-3}$]	$53.10^{+0.13}_{-0.11}$	$53.06^{+0.14}_{-0.11}$	$53.10^{+0.06}_{-0.05}$
log t_3 [K]	7.34 ± 0.10	7.26 ± 0.07	7.23 ± 0.01
EM $_3$ [cm $^{-3}$]	$52.93^{+0.20}_{-0.10}$	$53.04^{+0.10}_{-0.22}$	$52.28^{+0.23}_{-0.44}$
red. χ^2	0.73	0.62	0.94
DOF	709	589	1316
log L_X [erg s $^{-1}$]	30.51	30.52	30.61
log $\frac{L_X}{L_{bol}}$	-3.37	-3.36	-3.27

Note: the errors are estimated with 90% confidence limit.

4.2.2. Line based analysis

We identified the individual line features on the basis of CHIANTI version 4.02 (Dere et al. 2001) database. The identified lines and their corresponding fluxes are listed in Appendix. In Figure 1, both the MEG and HEG spectra are shown. The lines in the MEG spectra are much brighter than in the HEG spectra. Therefore, we consider only the lines seen in the MEG for further analysis.

We derive the differential emission measure (DEM) from the measured line fluxes using Markov Chain Monte Carlo (MCMC) analysis method of Kashyap & Drake (1998) as implemented in the PINTofALE² software package. The DEM gives the amount of plasma as a function of temperature. The MCMC analysis gives an estimate of emission measure distribution over a pre-selected range of temperatures with a DEM estimate for each of the temperature bins. We used a temperature grid with $\delta \log T = 0.05$ with a range of $6.2 < \log T [K] < 7.4$. All strong emission lines which are reasonably isolated (minimum separation $\sim 0.01 \text{ \AA}$) were used for the DEM reconstruction. We derived the abundance relative to the iron for all the elements for which at least one line has been identified and included in the selection. The elemental abundances were obtained along with reconstructed DEM distribution. For this, we used only the iron lines from our selection to obtain the initial DEM distribution and abundance of Fe. We then added the lines of other elements one by one gradually extending to the temperature range where the DEM is constrained. At each iteration, we obtained a new DEM distribution and the abundance relative the Fe abundance. Once the DEM distribution has been calculated the Fe abundance is determined by comparing the observed continuum with the predicted continuum based on different metallicity values (see Argiroffi et al. 2003).

In Figure 6, we show the reconstructed DEM for HD 155555 AB. The general shape of DEM distribution derived for HD 155555 AB for three time-intervals consistently shows a multi-temperature plasma with a dominant peak at $\log T [K] \sim 6.9-7.0$, very well constrained by line fluxes. This peak is consistent with the one of the temperature components predicted by XSPEC model. The peak at the low temperature between $\log T [K] \sim 6.35-$

² see <http://hea-www.harvard.edu/PINTofALE/>

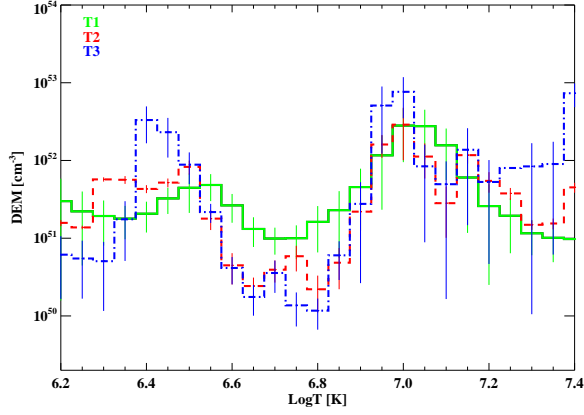


FIG. 6.— Best fit DEM plots versus the log T for HD 155555 AB. 6.55 is much more prominent during time interval T3 when compared to the other time intervals. During time interval T2 and T3, we notice a higher temperature component ($\log T[\text{K}] > 7.35$) which implies that the enhanced activity level during time interval T2 and T3 is adding a discrete source of emission at the higher and lower end of the temperature range.

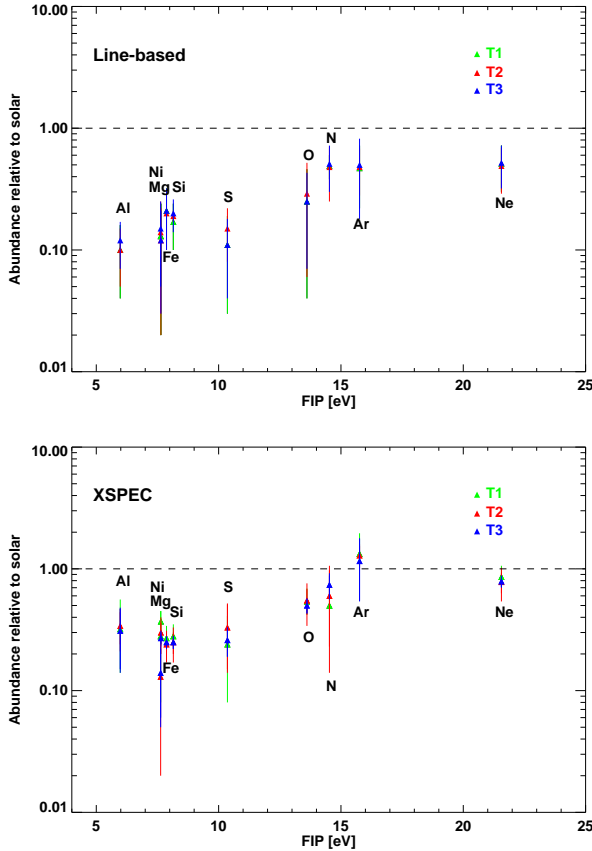


FIG. 7.— The coronal abundance relative to solar photospheric values (Grevesse & Sauval 1998) as derived by line-based (left panel) and XSPEC based analysis (right panel) for T1, T2 and T3 time bins plotted as a function of the first ionisation potential (FIP) for HD 155555 AB.

In Figure 7, the coronal elemental abundances of HD 155555 AB obtained for all the three time-intervals

are plotted as a function of the first ionisation potential of the elements. In Table 5, we list the coronal elemental abundances relative to the solar photospheric abundances derived by both the line based method and XSPEC fitting methods. The line-based and the XSPEC fitting to the MEG spectra give nearly consistent values for the elemental abundance except for Ar, despite the difference in the temperature distribution derived using the two methods. This could be because in the line-based analysis we reject lines that are blended and problematic whereas the XSPEC fitting assumes that the model can explain each and every individual line in the observed spectrum. Furthermore, we use 3T XSPEC model to characterise the corona which is a criterion we use to define a multi-temperature structure of the corona; whereas the DEM reconstruction shows clearly that the corona of HD 155555 AB has a continuously distributed multi-temperature thermal structure.

4.2.3. Optical depth effects

Generally, the X-ray emission from coronal plasmas can be assumed to be optically thin (Schrijver et al. 1995; Mewe et al. 1995). In order to justify the optically thin model used in our analysis, we estimated the optical depth by comparing the observed flux ratio of the Fe XVII line at 15.265 Å to the resonance line at 15.040 Å of Fe XVII but with a lower oscillator strength. These ratios have been measured in the laboratory using an electron beam ion trap by Brown et al. (1998) and the values range between 0.31-0.36 at 0.85-1.3 keV. The measured value for the Sun is 0.49 ± 0.05 (Saba et al. 1999). We obtained a ratio of 0.35 ± 0.11 for HD 155555 AB, which is larger than the value of 0.26 ± 0.10 determined for Capella (Brinkman et al. 2000) and smaller than the value of 0.49 ± 0.14 determined for II Peg (Huenemoerder et al. 2001). The uncertainty in the ratio for HD 155555 AB is large enough that the results are consistent with previously estimated ratios.

4.2.4. Electron densities

We have investigated the electron densities of the coronal plasma using the density-sensitive line flux ratios of forbidden to inter combination lines of helium-like triplets (N VI, O VII, Ne IX, Mg XI and Si XIII), based on the theory of density-sensitive lines as described in detail by Gabriel & Jordan (1969). The He-like triplets of O VII, Ne IX, Mg XI and Si XIII are strong enough in our observations to obtain characteristic electron densities in the source (see Figure 8). Note that in the second panel of Fig. 8, the Ne IX inter-combination line (13.553 Å) is blended with Fe XIX (13.518 Å), since the spectral resolution of *Chandra* HEG and MEG are 0.005 and 0.0025 Å per bin, respectively, the peaks are well-resolved and are easily fitted with two separate Gaussian components. The measured line counts, the f/i ratios and the deduced electron densities for the entire duration of observation are listed in Table 6. In order to convert the measured f/i ratios to densities, we approximated the flux ratio by

$$\frac{f}{i} = \frac{R_o}{1 + \frac{n_e}{N_c}}$$

where R_o is the low-density limit and N_c is the critical density for which we adopted the values from

TABLE 5
BEST FIT VALUES OF THE ELEMENTAL ABUNDANCES FOR DIFFERENT TIME INTERVALS.

Elements	T1		T2		T3	
	XSPEC	Line-based	XSPEC	Line-based	XSPEC	Line-based
N	0.50	0.49±0.11	0.60 ^{+0.37} _{-0.46}	0.48±0.23	0.74 ^{+0.18} _{-0.14}	0.51±0.21
O	0.54 ^{+0.15} _{-0.12}	0.25±0.21	0.55 ^{+0.21} _{-0.13}	0.29±0.23	0.50 ^{+0.07} _{-0.07}	0.25±0.18
Ne	0.86 ^{+0.20} _{-0.15}	0.51±0.21	0.78 ^{+0.24} _{-0.15}	0.49±0.20	0.79 ^{+0.09} _{-0.08}	0.52±0.20
Mg	0.37 ^{+0.08} _{-0.07}	0.13±0.11	0.30 ^{+0.10} _{-0.06}	0.12±0.10	0.27 ^{+0.04} _{-0.03}	0.12±0.09
Al	0.32 ^{+0.24} _{-0.18}	0.10±0.06	0.34 ^{+0.13} _{-0.10}	0.10±0.05	0.31 ^{+0.16} _{-0.17}	0.12±0.05
Si	0.28 ^{+0.07} _{-0.05}	0.17±0.07	0.25 ^{+0.08} _{-0.05}	0.19±0.02	0.25 ^{+0.03} _{-0.03}	0.20±0.06
S	0.24 ^{+0.17} _{-0.16}	0.11±0.08	0.33 ^{+0.19} _{-0.18}	0.14±0.07	0.26 ^{+0.07} _{-0.07}	0.11±0.07
Ar	1.33 ^{+0.63} _{-0.15}	0.47±0.25	1.29 ^{+0.30} _{-0.25}	0.48±0.20	1.16 ^{+0.62} _{-0.61}	0.50±0.32
Fe	0.27 ^{+0.07} _{-0.05}	0.21±0.11	0.24 ^{+0.07} _{-0.04}	0.20±0.10	0.25 ^{+0.03} _{-0.02}	0.21±0.11
Ni	0.28 ^{+0.17} _{-0.20}	0.13±0.11	0.13 ^{+0.21} _{-0.11}	0.14±0.11	0.14 ^{+0.09} _{-0.08}	0.15±0.10

Pradhan & Shull (1981) for each of the ions. Notice that f/i ratio and electron densities obtained from the dispersed spectrum represent mean values over the entire observation.

Furthermore, using the measured f , i and r line fluxes we have calculated the $G = \frac{f+i}{r}$ ratio for the time-averaged spectra, which provides an estimate of the electron temperature T_e . The dependence on temperatures of the G -ratios is due to the collisional excitations which have a different temperature sensitivity for the forbidden and inter-combination lines compared to the r lines. In the case of a strong r line the G -ratio ($G \sim 1$) suggests a collisionally dominated plasma (see Table 6). We compared the measured $G(T)$ values of O VII, Ne IX, Mg XI and Si XIII with the theoretical relation between the electron temperature and $G(T)$ as described by Porquet & Dubau (2000) and have plotted the results in Figure 9). The comparison shows that the coronal temperature is in 2-12 MK range. This temperature range is comparable to the temperatures derived using the DEM analysis.

We derived the R and G ratio for each of the time bins and refined the analysis of plasma temperature and density. In Figure 10, we show the line fluxes and their ratios as a function of time. Although individual fluxes clearly show an increasing trend during T3, the f/i ratio shows marginal variation between T1, T2 and T3.

The electron densities calculated using O VII triplets for HD 155555 AB time bins T1, T2 and T3 are $\log n_e [\text{cm}^{-3}] \sim 10.98^{+0.17}_{-0.98}$, $10.65^{+0.30}_{-0.74}$, and $10.66^{+0.17}_{-0.77}$, respectively at $\log T[\text{K}] \sim 6.3$. The Ne IX triplet is strongly affected by the blending of Fe XIX hence the obtained density might be highly uncertain; however, we obtain $\log n_e [\text{cm}^{-3}] \sim 11.79^{+1.23}_{-1.17}$, $11.87^{+0.83}_{-1.59}$, and $11.72^{+1.16}_{-0.74}$ for time bins T1, T2 and T3, respectively, at $\log T[\text{K}] \sim 6.6$. Higher densities are indicated by the Mg XI and Si XIII triplets yielding $\log n_e [\text{cm}^{-3}] \sim 12.73^{+1.23}_{-1.17}$, $12.68^{+0.32}_{-0.67}$, and $12.82^{+0.23}_{-0.90}$ at $\log T[\text{K}] \sim 6.9$ and $\log n_e [\text{cm}^{-3}] \sim 13.29^{+0.36}_{-0.52}$, $13.45^{+0.34}_{-0.58}$, and $13.44^{+0.27}_{-0.97}$ at $\log T[\text{K}] \sim 7.0$, for time bins T1, T2 and T3, respectively. Our results show that the electron densities are higher in the plasma region with higher temperature.

5. ANALYSIS AND RESULTS: HD 155555 C

We subjected the spectra of the M-dwarf companion to the same analysis that we have applied to HD 155555 AB,

as described in § 4.

5.1. Light curve

The X-ray light curve obtained in 0.4-6.0 keV range is shown in Figure 11. There is flare-like feature observed in HD 155555 C where the intensity increases by a factor of ~ 2 (Fig. 11). The flare like feature was fitted with an exponential function

$$CR(t) = A_0 e^{-\frac{(t-t_0)}{\tau_{r,d}}} \quad (1)$$

where $CR(t)$ is the count rate as a function of time, A_0 is the count rate at the flare peak, t_0 is the time of peak count rate, $\tau_{r,d}$ is the rise/decay time of the flare. The short rise ($\tau_r \sim 6.00 \pm 0.02$ ks) followed by a slow steady decline ($\tau_d \sim 8.90 \pm 0.03$ ks) in the X-ray counts are similar to the flares observed on pre-main sequence stars (Stelzer et al. 2005; Getman et al. 2008). We have examined the spectral evolution of HD 155555 C but there is no obvious spectral hardening during this flare-like feature (bottom panel of Fig. 11) based on hardness ratio variation. The enhancement in the emission could occur as a result of magnetic reconnection. Since there is an increase in the count rate and no apparent change in the hardness ratio or temperature, we can interpret this enhancement in two ways 1) the increase in count rate was a result of more plasma with similar coronal properties rotating into the line-of-sight or 2) there is indeed a change in the coronal temperature but could not be observed as a result of the relatively poor statistics of this spectrum.

5.2. Spectral analysis

The spectrum of the HD 155555 C is significantly softer than that of HD 155555 AB; this is evident clearly in the first-order spectrum (see Fig. 2). We have used multi-temperature VAPEC model assuming an optically thin coronal plasma to the dispersed spectrum of HD 155555 C. We fit two temperature component VAPEC models which produced a $\chi^2 \sim 232$ (DOF ~ 204). We then added an additional temperature component which produced a $\chi^2 \sim 164$ (DOF ~ 202). Based on the F-statistic we obtained a p-value of 0.008. We further added an additional temperature component which did not improve the chi-square significantly and produced an unambiguously large F-test p-value of 0.49. Hence we modelled the spectra of HD 155555 C with three temperature component allowing the abundance of

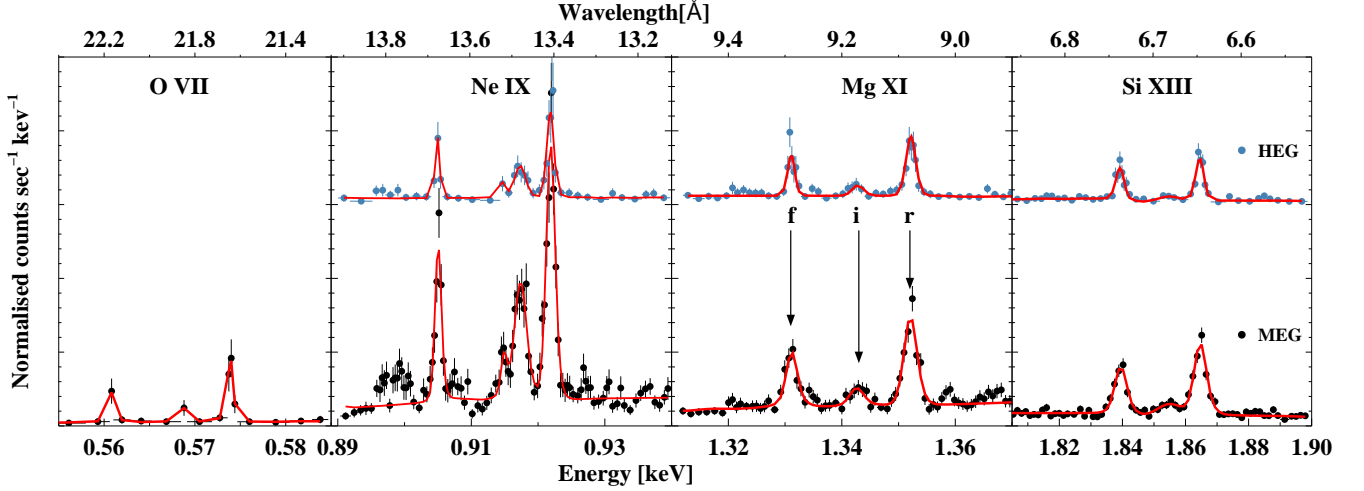


FIG. 8.— He-like triplets of O VII, Ne IX, Mg XI and Si XIII measured with the entire HEG and MEG spectra of HD 155555 AB with the line fits. The Gaussian used to fit the lines are shown in red.

TABLE 6
LINE FLUXES, LINE RATIOS AND DENSITIES FOR HE LIKE TRIPLETS OF THE TOTAL (TIME AVERAGED) HD 155555 AB SPECTRUM.

Ion	$G = \frac{f+i}{r}$	$\log(T_e)$ K	$R = \frac{f}{i}$	$\log(n_e)$ cm^{-3}
Si XIII	0.73 ± 0.12	6.92 ± 0.20	7.08 ± 1.18	$13.34^{+0.83}_{-0.67}$
Mg XI	0.73 ± 0.07	6.76 ± 0.17	1.95 ± 0.20	$12.72^{+0.95}_{-0.84}$
Ne IX	0.83 ± 0.10	6.48 ± 0.09	2.87 ± 0.34	$11.83^{+1.15}_{-1.08}$
O VII	0.82 ± 0.25	6.38 ± 0.22	1.13 ± 0.35	$10.80^{+0.81}_{-0.65}$

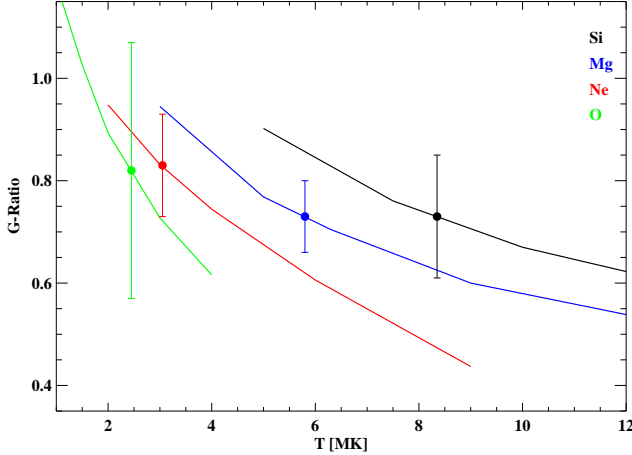


FIG. 9.— The G-ratio curve from Porquet & Dubau (2000) for O VII (in green), Ne IX (in red), Mg XI (in blue) and Si XIII (in black) plotted as a function of temperature. The filled circles represents the measured G-ratio for HD 155555 AB.

O, Ne, Mg, Si, S and Fe independently. The resultant model parameters are shown in Table 7. We estimate an unabsorbed X-ray flux of $\sim 1.89 \times 10^{-12} \text{ erg cm}^{-2} \text{ s}^{-1}$ for HD 155555 C which corresponds to X-ray luminosity of $2 \times 10^{29} \text{ erg s}^{-1}$. The abundances of X-ray emitting plasma obtained from the above model are listed in Table 8.

In addition to the global fits we have used the line-based analysis as in the case of HD 155555 AB to assess the coronal temperatures, emission measures and the abundances of HD 155555 C. We reconstructed the DEM using all the strong lines. The resulting DEM distribu-

TABLE 7
BEST-FIT SPECTRAL PARAMETERS OBTAINED FROM ITERATIVE FITTING OF DISPERSED X-RAY SPECTRA FOR HD 155555 C DATA USING 3T VAPEC PLASMA MODELS.

Parameters	
$\log t_1$ drive drive[K]	$6.49^{+0.12}_{-0.20}$
EM_1 [cm^{-3}]	$51.65^{+0.02}_{-0.03}$
$\log t_2$ [K]	$6.90^{+0.05}_{-0.12}$
EM_2 [cm^{-3}]	$51.71^{+0.08}_{-0.09}$
$\log t_3$ [K]	$7.34^{+0.05}_{-0.04}$
EM_3 [cm^{-3}]	$51.86^{+0.09}_{-0.10}$
red. χ^2	0.81
DOF	202
$\log L_x$ [$erg s^{-1}$]	29.30

Note: the errors are estimated with 90% confidence limit.

TABLE 8
ABUNDANCES MEASUREMENTS FOR HD 155555 C.

Elements	HD 155555 C	
	XSPEC	Line-based
O	$0.31^{+0.39}_{-0.18}$	0.29 ± 0.06
Ne	$0.92^{+1.03}_{-0.90}$	0.89 ± 0.45
Mg	$0.36^{+0.17}_{-0.06}$	0.27 ± 0.15
Al	0.5	0.45 ± 0.31
Si	$0.48^{+0.28}_{-0.22}$	0.29 ± 0.10
S	$0.55^{+0.30}_{-0.24}$	0.35 ± 0.12
Fe	$0.50^{+0.33}_{-0.20}$	0.41 ± 0.14

tion is shown in Figure 12 peaking at $\log T[K] \sim 6.3$. The elemental abundances were also determined using the reconstructed DEM and their values are given in Table 8.

We estimated the coronal density using density-sensitive ratio of forbidden and inter-combination lines of Ne IX triplet and obtained a value of $\log N_e \sim 11.78^{+0.57}_{-0.23}$

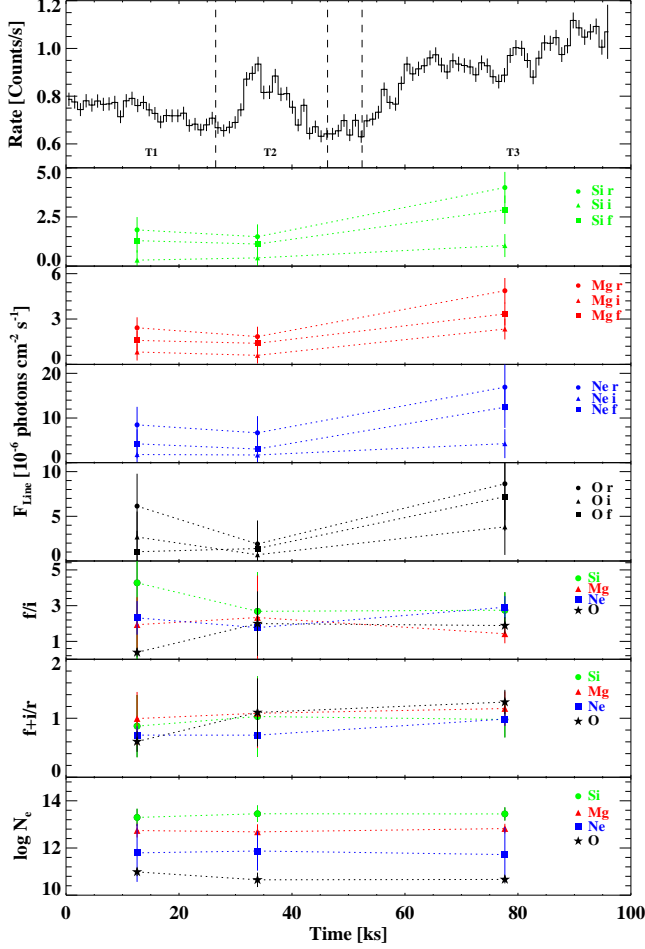


FIG. 10.— He-like triplets line fluxes of HD 155555 AB, their ratios and the densities as a function of time.

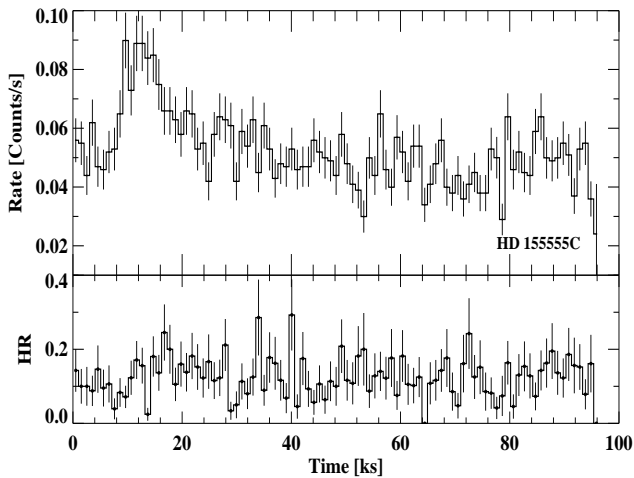


FIG. 11.— Background subtracted X-ray light curve in 0.4–6.0 keV energy band (top panel) and the hardness ratios as a function of time (bottom panel) for HD 155555 C.

(Table 9). Using the line fluxes of Si XIII, Mg XI and O VII we estimate an upper limit to the coronal densities of these elements (Table 9).

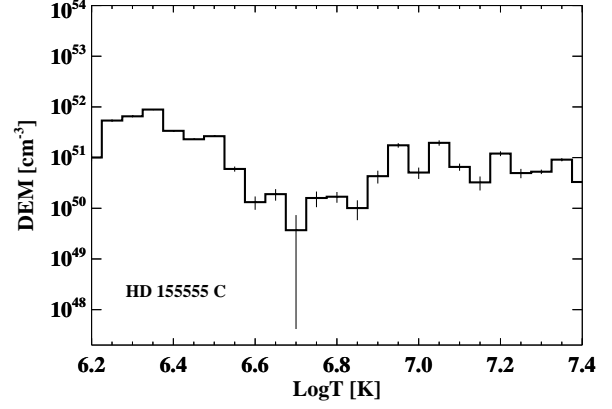


FIG. 12.— Best fit DEM plots versus the log T for HD 155555 C.

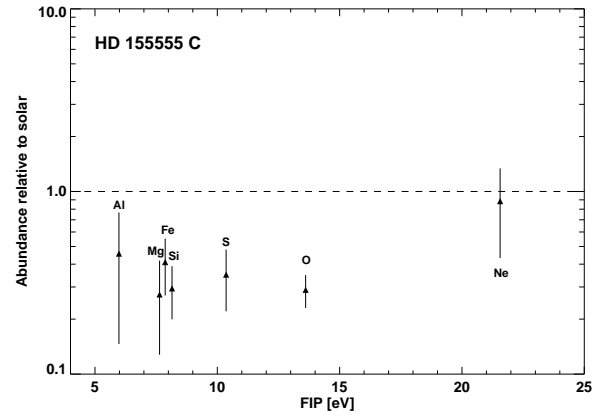


FIG. 13.— The coronal abundance relative to the solar photospheric values (Grevesse & Sauval 1998) as derived by line-based analysis are plotted as a function of the first ionisation potential (FIP) for HD 155555 C.

The ratio of Fe XVII resonance line at 15.01 Å and the adjacent line at 15.26 Å yielded 0.38 ± 0.25 , indicating a ratio similar to HD 155555 AB.

6. DISCUSSION

Our observation of HD 155555 AB shows continuous variability such that no part of the observation can be defined as being “quiescent” (see Fig. 3). The light curve was divided into three different time intervals. Interval T1 shows small-scale fluctuations and a steady decline which is perhaps indicative of the rotational modulation. During interval T2, a flare-like event is observed. The flare intensity is correlated with the hardness ratio. During interval T3, a steady rise with several small-scale variations is seen. This could be the result of one of the binary components crossing a large active region or several such regions on the stellar surface.

Our analysis of the *Chandra* HETG spectra has provided an insight into the plasma emission measure distribution, coronal temperatures, the abundances of individual elements, and the plasma densities as determined by He-like triplets. An obvious feature of the reconstructed DEMs (Fig. 6) for each time interval is the apparent bi-modal structure at similar temperatures. By comparing the XSPEC models predicting the observed spectra during three different time bins we find an increase in the

TABLE 9
LINE FLUXES, LINE RATIOS AND DENSITY FOR HE LIKE TRIPLETS OF HD 155555 C.

Ion	f	i	r	$G = \frac{f+i}{r}$	$\log(T_e)$ K	$R = \frac{f}{i}$	$\log(n_e)$ cm^{-3}
	[counts]	[counts]	[counts]				
Si XIII	9.63 ± 4.22	< 3.27	28.23 ± 6.38	< 0.45	...	< 2.94	< 13.42
Mg XI	26.30 ± 6.20	< 8.49	15.59 ± 5.04	< 2.23	...	< 3.09	< 12.59
Ne IX	22.28 ± 5.79	9.25 ± 4.16	13.63 ± 4.79	2.31 ± 1.14	...	2.40 ± 1.25	$11.78^{+0.57}_{-0.23}$
O VII	4.48 ± 3.28	< 2.43	< 5.49	< 1.25	...	< 1.84	< 10.67

source luminosity from 3.2×10^{30} erg s $^{-1}$ (during T1) to 4.1×10^{30} erg s $^{-1}$ (during T3). This is also reflected in the DEMs where the high-temperature peak at $\log T[K] \sim 6.9-7.0$ is higher during T3 by a factor 1.5-2 when compared to that during T1. The high-temperature peak values of the DEM are consistent with the values obtained using XSPEC. The peaks of the low-temperature components of the DEM (at $\log T[K] \sim 6.3-6.5$) increase by factors of 2-10 for T2 and T3 compared to T1. The large emission measure can be a result of an increase in the density or increase in the emitting volume.

A key parameter to interpret magnetically confined coronal structure is the plasma density. The measurements of the density and temperature obtained from the detailed analysis of He-like triplets allow us to estimate the volume and thus the average pressure of the emitting coronal region where these He-like triplets are formed. In Figure 14, we plot the estimated plasma pressure obtained using the densities and temperatures derived from the triplet line ratios as a function of the temperature. The plasma pressure increases steeply with increase in the temperature. A similar trend has been observed previously by Argiroffi et al. (2003) and Sanz-Forcada et al. (2003); they interpret this due to the presence of different kinds of coronal structures in different isobaric conditions where the plasma pressure increases for increasing temperature of the confined plasma but the volume filling factor decreases.

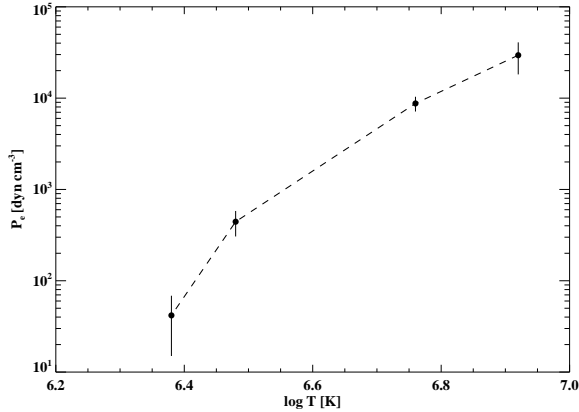


FIG. 14.— Electron pressure derived from the measured electron densities at different temperatures.

Stellar coronae often exhibit abundance anomaly patterns. A few moderately active, and even some low activity stars like the Sun, show an enhancement of low FIP elements and a depletion of high FIP elements. Highly active stars, on the other hand, exhibit an inverse pattern with the depletion of low-FIP elements and enhancement of high-FIP elements (inverse-FIP or iFIP effect).

These effects result in higher metallicities in the coronae of stars with low activity compared to high activity stars (Güdel et al. 2001). The abundances derived for HD 155555 AB by the two methods used here (see §4.2.1 and §4.2.2) show a general sub-solar abundance for most of the elements, though the low FIP elements (< 10 eV; e.g. Mg, Si, Fe) are depleted more compared to the high FIP elements (> 10 eV; e.g. O, Ne, Ar, N) (Fig. 7). The coronal abundances of HD 155555 AB relative to solar photospheric values (Grevesse & Sauval 1998), do not show a strong FIP dependence, but rather suggest a moderate iFIP effect. We do not see any strong variation in the individual abundances during different time intervals in HD 155555 AB, indicating that there is no significantly fresh chromospheric material being evaporated into the corona.

6.1. Comparison with other stars

In order to check whether there are any differences between the coronae of stars that are active due to their extreme youth and those in RS CVn binary systems that have been spun up by tidal forces, we compare the spectrum of HD 155555 AB with that of active stars and young stars, viz., AR Lac (an active RS CVn type binary), AB Dor (an active PMS star), HD 98800 (a WTTS), and TW Hya (a CTTS). AR Lac is one of the brightest RS CVn type binary (Siviero et al. 2006; Drake et al. 2014) with an orbital period of 1.98 d and with its binary components separated by $\sim 9.2 R_{\odot}$ (Chambliss 1976; Popper & Ulrich 1977). AB Dor is a bright ($V \approx 6.9$) young (age $\sim 30-100$ Myr) ultra-fast rotating ($P_{rot} \sim 0.52$ d) late-type star (Amado et al. 2001; Guirado et al. 2011 and references therein), and a member of a wide visual binary system (its companion is Rst 137B at a separation of $9''$ with spectral type M3-M5; Guirado et al. 2011). AB Dor is a highly active star that has been observed by many space-based observatories across the UV, EUV and X-ray wavelengths (Sanz-Forcada et al. 2003; García-Alvarez et al. 2008; Lalitha & Schmitt 2013). TW Hya is a low-mass K-type star with an age of < 10 Myr. TW Hya is accreting from its circumstellar disk (accretion rate of $\sim 1.0 \times 10^{-9}$ and $5 \times 10^{-8} M_{\odot} \text{ yr}^{-1}$; Batalha et al. 2002; Brickhouse et al. 2010), which may give rise to post-shock plasma. Therefore, we have also chosen a non-accreting X-ray bright PMS star, HD 98800 for comparison. TW Hya is a single CTTS, whereas HD 98800 is a multiple system with two visual components separated by $0.8''$ and orbital period of 300-400 years (Soderblom et al. 1998; Tokovinin 1999; Prato et al. 2001; Boden et al. 2005). The two components of HD 98800 are well resolved in the *Chandra* HETG zeroth-order image with the primary component HD 98800 A appearing to be ~ 4 times brighter than HD 98800 B (Kastner et al. 2004). This system displays an X-ray luminosity similar to TW Hya, however, there

is no evidence of accretion in HD 98800 (Kastner et al. 1997, 2004).

The basic stellar and X-ray properties of these stars are summarized in Table 10. The coronal emission of AR Lac, TW Hya and HD 98800 has been studied in detail via *Chandra* HETG observations (Batalha et al. 2002; Huenemoerder et al. 2004; Kastner et al. 2004; Drake et al. 2014). In Figure 15, we show the *Chandra* HETG spectra in the 13–16 Å region for AR Lac, AB Dor, HD 155555 AB, TW Hya and HD 98800. This wavelength region encompasses several highly ionised Fe lines and the Ne IX triplets. Visual comparison shows that the spectrum of HD 155555 AB is very similar to that of AR Lac and AB Dor showing similar relative line strengths for the Ne IX triplet and the Fe lines. On the other hand, TW Hya and HD 98800 show the Ne IX resonance line to be strong, and Fe lines to be weak compared to HD 155555 AB, AR Lac, and AB Dor.

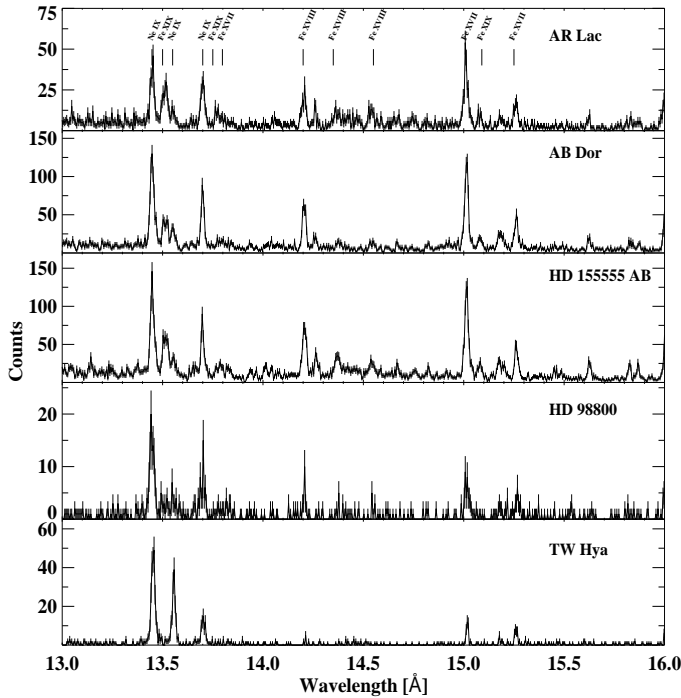


FIG. 15.— *Chandra* HETG spectra of the active late-type star AR Lac, young active stars AB Dor, HD 155555 AB, the pre-main sequence stars HD 98800 (WTTS) and TW Hya (CTTS), in the spectral region encompassing of Ne IX He-like triplets and Fe XVII lines.

Comparison of our results with AR Lac, AB Dor, TW Hya, and HD 98800 indicate that HD 155555 AB is very similar to AR Lac and AB Dor in its emission measure distribution, abundances, and electron densities, despite the difference in their ages. During flare-like events the emission measures peak at similar temperatures ($\log T[K] \sim 6.3$ and 6.9) for HD 155555 AB, AR Lac (Huenemoerder 2002) and AB Dor (Sanz-Forcada et al. 2003). However, an additional higher temperature component are observed during both quiescence and flare at $\log T[K] \sim$ for AB Dor. This difference in the temperatures could be due to the rapid rotation of AB Dor (Randich 1998) or due to its higher activity level (Telleschi et al. 2005). We note that the DEM distribu-

tions for both AR Lac and AB Dor are trimodal, whereas this is the case only during flare-like events (T2) for HD 155555 AB.

The total emission measure for the higher temperature component ($\log T[K] \sim 6.9$) is $\sim 52.35^{+0.08}_{-0.06} \text{ cm}^{-3}$ for HD 155555 AB, cf., $\sim 52.95^{+0.05}_{-0.06}$ and $\sim 52.34^{+0.03}_{-0.07} \text{ cm}^{-3}$ for AR Lac and AB Dor, respectively (Huenemoerder 2002; Sanz-Forcada et al. 2003). For TW Hya and HD 98800, there is no emission component at $\log T[K] \sim 6.9$. The DEM for TW Hya peaks at $\log T[K] \sim 6.5$ (Kastner et al. 2002) with no evidence of a hotter component ($\log T[K] > 7.0$). Similarly the DEM for HD 98800 has one peak at $\log T[K] \sim 6.5$, and a flat DEM thereafter (Huenemoerder et al. 2004; Kastner et al. 2004).

Güdel et al. (1997) studied a sample of solar-like G stars with ages ranging from 70–9000 Myr and found that the emission measure of the hotter component rapidly decreases with age. Our study, however, shows that the emission measures of the hotter component for HD 155555 AB and AB Dor are very similar with no noticeable trend. We note that the age of HD 155555 AB is several Myr younger than the youngest star (EK Dra, age ~ 70 Myr) in the sample compiled by Güdel et al. (1997). A more detailed analysis and interpretation of the coronal temperatures, emission measures, and densities of K-type stars with a range of ages is required in order to characterise how the X-ray properties of these stars evolve with time, and how their behaviour compares with solar-type stars.

The ratio of Ne to Fe abundance is ~ 3 for HD 155555 AB, ~ 5 for AR Lac (Huenemoerder 2002), ~ 5 for AB Dor (Sanz-Forcada et al. 2003) and ~ 5 for HD 98800 (Kastner et al. 2004), whereas this ratio is larger than the solar value by a factor of 10 for TW Hya (Kastner et al. 2002). Although the DEM peaks are similar for TW Hya and HD 98800, the Ne/Fe abundance ratio for HD 98800 is unlike that seen in TW Hya. This large ratio in TW Hya could be the result of an ongoing accretion where significant fractionation occurs in the circumstellar disk.

The electron densities ($\log n_e$) obtained for HD 155555 AB with O VII and Ne IX are 10.80 and 11.83 cm^{-3} , respectively, which are similar to the values for AR Lac (Huenemoerder 2002) and AB Dor (Sanz-Forcada et al. 2003; Lalitha et al. 2013). However, the $\log n_e$ values for O VII and Ne IX in TW Hya are 11.75 and 12.47 cm^{-3} respectively (Kastner et al. 2002). This could be the result of ongoing accretion seen in TW Hya (Argiroffi et al. 2009; Brickhouse et al. 2010; Dupree et al. 2012; Ness & Schmitt 2005).

Similarly, we have compared our results on HD 155555 C with other studies of M stars. In Figure 16, we show the *Chandra* HETG spectra in the 13–16 Å region for HD 155555 C, AU Mic and EQ Peg. AU Mic is an active nearby (distance ~ 10 pc) M type star showing typical X-ray luminosity of $2 \times 10^{29} \text{ ergs s}^{-1}$, similar to that of HD 155555 C (Rodono et al. 1986; Del Zanna et al. 2002). EQ Peg is a visual binary consisting of two stars with spectral type M3.5 and M4.5 which are separated by ≈ 30 AU. At a distance of 6.1 pc, the quiescent X-ray luminosity of EQ Peg has been measured to be between $6\text{--}7 \times 10^{28} \text{ ergs s}^{-1}$ (Robrade & Schmitt 2005). EQ Peg has a spectral type similar to that of HD 155555 C,

TABLE 10
COMPARISON OF PHYSICAL PROPERTIES OF AR LAC, AB DOR, HD 155555 AB, HD 98800 AND TW HYA.

Star	Spectral Type	Age Myr	Binarity	Ongoing Accretion	$P_{rot/orb}$ days	Distance	$\log L_x$	$\log \frac{L_x}{L_{bol}}$	T MK
AR Lac	K0IV+G5IV	$>3000^1$	Y	N	1.98	~ 43	30.89	-3.45	~ 16
AB Dor	K0-2V	30-100	Y	N	0.52	~ 15	30.01	-3.00	~ 13
HD 155555 AB	G5IV+K0IV	18	Y	N	1.68	~ 31	30.60	-3.28	~ 12
HD 98800	K4V	10	Y	N	262	~ 40	29.83	-3.40	2.5-10
TW Hya	K6Ve	8	N	Y	4.5?	~ 57	30.11	-2.92	~ 3

Note: The ages, spectral types and distances are from 1) Lanza et al. 1998; Drake et al. 2014, and references therein, for AR Lac; 2) Guirado et al. 2011 and references therein for AB Dor; 3) Strassmeier & Rice 2000 for HD 155555 AB; 4) Kastner et al. 1997; Webb et al. 1999 for HD 98800; 5) Batalha et al. 2002; Setiawan et al. 2008 for TW Hya. For AB Dor, $P_{rot/orb}$ listed in column 6 represents the rotation period (Guirado et al. 2011), whereas, for HD 98800 this value represents the orbital period of the wide binary (Boden et al. 2005). For AR Lac and HD 155555 AB, $P_{rot/orb}$ represents both rotation period and the orbital period since these systems are tidally locked (Lanza et al. 1998; Strassmeier & Rice 2000). For TW Hya, $P_{rot/orb}$ listed in column 6 represents an uncertain rotation period (Alencar & Batalha 2002). The coronal temperature (T) are the emission measure weighted temperatures in MK. For AR Lac and AB Dor the temperature and emission measures are obtained from Singh et al. (1996) and Lalitha et al. (2013), respectively. For TW Hya and HD 98800, the temperatures are obtained from Kastner et al. (2002) and Kastner et al. (2004), respectively.

and AU Mic shows X-ray emission similar to that of HD 155555 C. Visual comparison of Figure 16 shows that the spectrum of HD 155555 C shows a strong flux at 15.01 Å similar to what is seen in EQ Peg and AU Mic. The Ne IX triplet emission which is very strong in both EQ Peg and AU Mic is barely visible in the case of HD 155555 C. Although the Ne IX line luminosity for HD 155555 C is at least half an order of magnitude brighter than that of AU Mic, the Ne/Fe abundance ratio is ~ 2 , whereas for AU Mic and EQ Peg the ratios are ~ 7 and ~ 8 , respectively.

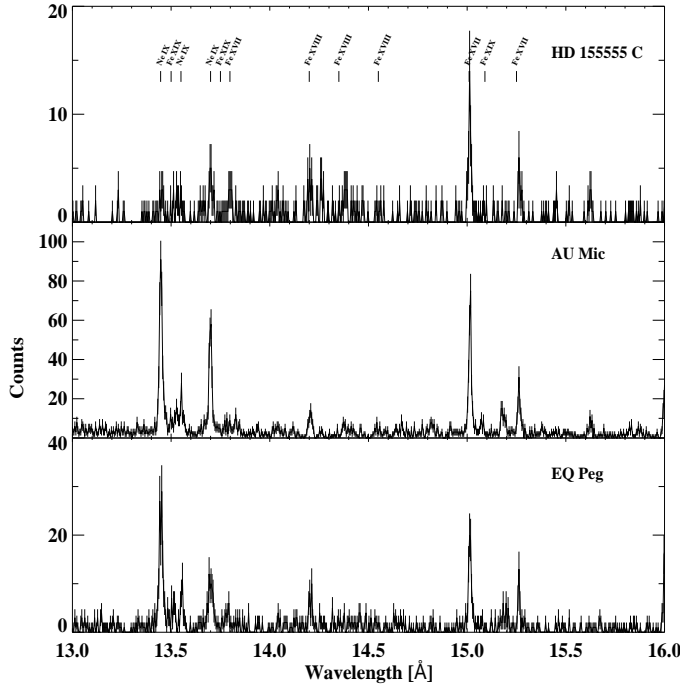


FIG. 16.— *Chandra* HETG spectra of HD 155555 C and the active late-type M stars AU Mic and EQ Peg with similar spectral type as HD 155555 C system, in the spectral region encompassing of Ne IX He-like triplets and Fe XVII lines.

The emission measure of HD 155555 C shows a peak at $\log T[K] \sim 6.4$, and has no significant plasma emission at $\log T[K] \sim 7$. In contrast, AU Mic and EQ Peg show peaks around $\log T[K] \sim 6.8-6.9$ with the bulk of the plasma lo-

cated between $\log T[K] \sim 6.3-7.3$. However, the temperatures and emission measures obtained by XSPEC model fit are consistent with the results obtained for AU Mic and EQ Peg. The abundances of HD 155555 C show a moderate iFIP effect, which is common among stars with high activity levels like AU Mic and EQ Peg. The metallicities of HD 155555 C found here are sub-solar.

7. CONCLUSION

We have analysed the *Chandra* HETG data of a young active multiple system, HD 155555. We infer the following characteristics of the coronal plasma of this system:

- The X-ray emission shows continuous variability throughout the observation, with flare-like events. The light curve also shows a possible modulation due to coronal hot spots. Since the observation reported here spans only $\sim 65\%$ ($P_{rot} \sim 1.68d$ and $P_{obs} \sim 1.09d$) of the rotation period, additional observations covering at least a few rotation periods of HD 155555 AB are required to verify whether the observed variation is indeed due to rotational modulation.
- The emission measure distributions calculated for the coronal plasma of HD 155555 AB and HD 155555 C using individual line fluxes, show a stable structure at $\log(T) = 6.4$ followed by a steep increase up to the peak at $\log(T) = 6.9$. During high activity state the DEM shows an increase in the amount of X-ray emission. For HD 155555 C, the DEM shows a peak at $\log(T) = 6.3$, followed by a plateau in the range $\log(T) = 6.9-7.4$.
- Element abundances in the corona of HD 155555 AB and HD 155555 C are observed to follow an intermediate behavior between the solar-like FIP effect, and the inverse FIP effect observed in other active stars. The coronal metallicity in both the HD 155555 AB and C spectra is sub-solar, as is typically found in active stars.
- The continuum, line emissivity, densities and the temperatures of the coronal plasma in HD 155555 AB, are very similar to that of other active stars of similar age, like AB Dor and older RS CVns, like AR Lac, but very different from that of

other young stars of CTTS or WTTS type. These results thus indicate that age has little effect on their activity, unlike what is seen in the solar-type stars. A detailed study of a range of K-type stars with different ages, however, may reveal the dependence of coronal properties on age, and whether the

behaviour is similar to the solar-type stars or not.

- The X-ray emission of the HD 155555 C component is similar to that of other M-type dwarf stars of similar activity levels in the solar neighborhood.

REFERENCES

- Alencar, S. H. P., & Batalha, C. 2002, *ApJ*, 571, 378
- Amado, P. J., Cutispoto, G., Lanza, A. F., & Rodonò, M. 2001, in *Astronomical Society of the Pacific Conference Series*, Vol. 223, 11th Cambridge Workshop on Cool Stars, Stellar Systems and the Sun, ed. R. J. Garcia Lopez, R. Rebolo, & M. R. Zapaterio Osorio, 895
- Argiroffi, C., Maggio, A., & Peres, G. 2003, *A&A*, 404, 1033
- Argiroffi, C., Maggio, A., Peres, G., Drake, J. J., López-Santiago, J., Sciortino, S., & Stelzer, B. 2009, *A&A*, 507, 939
- Arnaud, K. A. 1996, in *ASP Conf. Ser. 101: Astronomical Data Analysis Software and Systems V*, ed. G. H. Jacoby & J. Barnes, 17
- Audard, M., Güdel, M., Sres, A., Mewe, R., Raassen, A. J. J., Behar, E., Foley, C. R., & van der Meer, R. L. J. 2002, in *Astronomical Society of the Pacific Conference Series*, Vol. 277, *Stellar Coronae in the Chandra and XMM-NEWTON Era*, ed. F. Favata & J. J. Drake, 65
- Audard, M., Güdel, M., Sres, A., Raassen, A. J. J., & Mewe, R. 2003, *A&A*, 398, 1137
- Ball, B., Drake, J. J., Lin, L., Kashyap, V., Laming, J. M., & García-Alvarez, D. 2005, *ApJ*, 634, 1336
- Barstow, M. A. 1987, *MNRAS*, 228, 251
- Batalha, C., Batalha, N. M., Alencar, S. H. P., Lopes, D. F., & Duarte, E. S. 2002, *ApJ*, 580, 343
- Boden, A. F., et al. 2005, *ApJ*, 635, 442
- Brickhouse, N. S., Cranmer, S. R., Dupree, A. K., Luna, G. J. M., & Wolk, S. 2010, *ApJ*, 710, 1835
- Brinkman, A. C., et al. 2001, *A&A*, 365, L324
- Brinkman, A. C., et al. 2000, *ApJ*, 530, L111
- Bromage, G. E., Kellett, B. J., Jeffries, R. D., Innis, J. L., Matthews, L., Anders, G. J., & Coates, D. W. 1992, in *Astronomical Society of the Pacific Conference Series*, Vol. 26, *Cool Stars, Stellar Systems, and the Sun*, ed. M. S. Giampapa & J. A. Bookbinder, 80
- Brown, G. V., Beiersdorfer, P., Liedahl, D. A., Widmann, K., & Kahn, S. M. 1998, *ApJ*, 502, 1015
- Chambliss, C. R. 1976, *PASP*, 88, 762
- Cutispoto, G. 1990, *A&AS*, 84, 397
- Del Zanna, G., Landini, M., & Mason, H. E. 2002, *A&A*, 385, 968
- Drake, J. J., & Kashyap, V. 2001, *ApJ*, 547, 428
- Drake, J. J., Ratzlaff, P., Kashyap, V., Huenemoerder, D. P., Wargelin, B. J., & Pease, D. O. 2014, *ApJ*, 783, 2
- Drake, S. A., Osten, R. A., Krimm, H., De Pasquale, M., Gehrels, N., & Barthelmy, S. 2015, *The Astronomer's Telegram*, 6940, 1
- Dunstone, N. J., Hussain, G. A. J., Collier Cameron, A., Marsden, S. C., Jardine, M., Barnes, J. R., Ramirez Velez, J. C., & Donati, J.-F. 2008, *MNRAS*, 387, 1525
- Dupree, A. K., et al. 2012, *ApJ*, 750, 73
- Flaccomio, E., Micela, G., Favata, F., & Alencar, S. P. H. 2010, *A&A*, 516, L8
- Fuhrmeister, B., Lalitha, S., Poppenhaeger, K., Rudolf, N., Liefke, C., Reiners, A., Schmitt, J. H. M. M., & Ness, J.-U. 2011, *A&A*, 534, A133
- Gabriel, A. H., & Jordan, C. 1969, *MNRAS*, 145, 241
- García-Alvarez, D., Drake, J. J., Kashyap, V. L., Lin, L., & Ball, B. 2008, *ApJ*, 679, 1509
- Garmire, G. P., Bautz, M. W., Ford, P. G., Nousek, J. A., & Ricker, G. R., Jr. 2003, in *Society of Photo-Optical Instrumentation Engineers (SPIE) Conference Series*, Vol. 4851, *X-Ray and Gamma-Ray Telescopes and Instruments for Astronomy*, ed. J. E. Truemper & H. D. Tananbaum, 28
- Getman, K. V., Feigelson, E. D., Broos, P. S., Micela, G., & Garmire, G. P. 2008, *ApJ*, 688, 418
- Grevesse, N., & Sauval, A. J. 1998, *Space Sci. Rev.*, 85, 161
- Güdel, M., et al. 2001, *A&A*, 365, L336
- Güdel, M., et al. 2007, *A&A*, 468, 353
- Güdel, M., Guinan, E. F., & Skinner, S. L. 1997, *ApJ*, 483, 947
- Güdel, M., & Nazé, Y. 2009, *A&A Rev.*, 17, 309
- Güdel, M., Skinner, S. L., Briggs, K. R., Audard, M., Arzner, K., & Telleschi, A. 2005, *ApJ*, 626, L53
- Guirado, J. C., Marcaide, J. M., Martí-Vidal, I., Le Bouquin, J.-B., Close, L. M., Cotton, W. D., & Montalbán, J. 2011, *A&A*, 533, A106
- Hall, D. S. 1980, *ApJ*, 236, L137
- Huenemoerder, D. P. 2002, in *High Resolution X-ray Spectroscopy with XMM-Newton and Chandra*, ed. G. Branduardi-Raymont, 18
- Huenemoerder, D. P., Boroson, B., Schulz, N. S., Canizares, C. R., Buzasi, D. L., Preston, H. L., & Kastner, J. H. 2004, in *IAU Symposium*, Vol. 219, *Stars as Suns : Activity, Evolution and Planets*, ed. A. K. Dupree & A. O. Benz, 238
- Huenemoerder, D. P., Canizares, C. R., & Schulz, N. S. 2001, *ApJ*, 559, 1135
- Kashyap, V., & Drake, J. J. 1998, *ApJ*, 503, 450
- Kastner, J. H., Huenemoerder, D. P., Schulz, N. S., Canizares, C. R., Li, J., & Weintraub, D. A. 2004, *ApJ*, 605, L49
- Kastner, J. H., Huenemoerder, D. P., Schulz, N. S., Canizares, C. R., & Weintraub, D. A. 2002, *ApJ*, 567, 434
- Kastner, J. H., Zuckerman, B., Weintraub, D. A., & Forveille, T. 1997, *Science*, 277, 67
- Lalitha, S., Fuhrmeister, B., Wolter, U., Schmitt, J. H. M. M., Engels, D., & Wieringa, M. H. 2013, *A&A*
- Lalitha, S., & Schmitt, J. H. M. M. 2013, *A&A*
- Lanza, A. F., Catalano, S., Cutispoto, G., Pagano, I., & Rodono, M. 1998, *A&A*, 332, 541
- Little-Marein, I. R., Simon, T., Ayres, T. R., Cohen, N. L., Feldman, P. A., Linsky, J. L., Little, S. J., & Lyons, R. 1986, *ApJ*, 303, 780
- Martin, E. L., & Brandner, W. 1995, *A&A*, 294, 744
- Mewe, R., Kaastra, J. S., Schrijver, C. J., van den Oord, G. H. J., & Alkemade, F. J. M. 1995, *A&A*, 296, 477
- Ness, J.-U., & Schmitt, J. H. M. M. 2005, *A&A*, 444, L41
- Pasquini, L., Cutispoto, G., Gratton, R., & Mayor, M. 1991, *A&A*, 248, 72
- Pasquini, L., Schmitt, J. H. M. M., Harnden, F. R., Jr., Tozzi, G. P., & Krautter, J. 1989, *A&A*, 218, 187
- Popper, D. M., & Ulrich, R. K. 1977, *ApJ*, 212, L131
- Porquet, D., & Dubau, J. 2000, *A&AS*, 143, 495
- Pradhan, A. K., & Shull, J. M. 1981, *ApJ*, 249, 821
- Prato, L., et al. 2001, *ApJ*, 549, 590
- Protassov, R., van Dyk, D. A., Connors, A., Kashyap, V. L., & Siemiginowska, A. 2002, *ApJ*, 571, 545
- Randich, S. 1998, in *Astronomical Society of the Pacific Conference Series*, Vol. 154, *Cool Stars, Stellar Systems, and the Sun*, ed. R. A. Donahue & J. A. Bookbinder, 501
- Reale, F., Betta, R., Peres, G., Serio, S., & McTiernan, J. 1997, *A&A*, 325, 782
- Robrade, J., & Schmitt, J. H. M. M. 2005, *A&A*, 435, 1073
- Rodonò, M., et al. 1986, *A&A*, 165, 135
- Rucinski, S. M. 1982, *Information Bulletin on Variable Stars*, 2203, 1
- Saba, J. L. R., Schmelz, J. T., Bhatia, A. K., & Strong, K. T. 1999, *ApJ*, 510, 1064
- Sanz-Forcada, J., Maggio, A., & Micela, G. 2003, *A&A*, 408, 1087
- Schrijver, C. J., Mewe, R., van den Oord, G. H. J., & Kaastra, J. S. 1995, *A&A*, 302, 438
- Setiawan, J., Henning, T., Launhardt, R., Müller, A., Weise, P., & Kürster, M. 2008, *Nature*, 451, 38
- Singh, K. P., Drake, S. A., & White, N. E. 1996, *AJ*, 111, 2415
- Singh, K. P., White, N. E., & Drake, S. A. 1996, *ApJ*, 456, 766
- Siviero, A., Dallaporta, S., & Munari, U. 2006, *Baltic Astronomy*, 15, 387
- Skinner, S. L., Audard, M., & Güdel, M. 2011, *ApJ*, 737, 19

- Smith, R. K., Brickhouse, N. S., Liedahl, D. A., & Raymond, J. C. 2001, *ApJ*, 556, L91
- Soderblom, D. R., et al. 1998, *ApJ*, 498, 385
- Stelzer, B., Flaccomio, E., Montmerle, T., Micela, G., Sciortino, S., Favata, F., Preibisch, T., & Feigelson, E. D. 2005, *ApJS*, 160, 557
- Stelzer, B., Hubrig, S., Orlando, S., Micela, G., Mikulášek, Z., & Schöller, M. 2009, *A&A*, 499, 529
- Strassmeier, K. G., & Rice, J. B. 2000, *A&A*, 360, 1019
- Telleschi, A., Güdel, M., Briggs, K., Audard, M., Ness, J.-U., & Skinner, S. L. 2005, *ApJ*, 622, 653
- Tokovinin, A. A. 1999, *Astronomy Letters*, 25, 669
- Walter, F. M., & Bowyer, S. 1981, *ApJ*, 245, 671
- Walter, F. M., Bowyer, S., Linsky, J. L., & Garmire, G. 1980, *ApJ*, 236, L137
- Webb, R. A., Zuckerman, B., Platais, I., Patience, J., White, R. J., Schwartz, M. J., & McCarthy, C. 1999, *ApJ*, 512, L63
- Weisskopf, M. C., Brinkman, B., Canizares, C., Garmire, G., Murray, S., & Van Speybroeck, L. P. 2002, *PASP*, 114, 1

APPENDIX

TABLE 11
LINE IDENTIFICATION AND LINE FLUXES FOR THE ENTIRE HD 155555 AB SPECTRA AND HD 155555 C SPECTRA.

Ion	log T_{max} [K]	Transition [upper \rightarrow lower]	λ_{pred} [Å]	HD 155555 AB		HD 155555 C	
				λ_{obs} [Å]	F_l [counts]	λ_{obs} [Å]	F_l [counts]
Ar XVIII	7.60	Unknown	3.727	3.727	35.93 \pm 7.05
Ar XVI	7.20	Unknown	3.952	3.951	52.68 \pm 8.30
Ar XVI/XVII	7.20/7.30	Unknown	3.994	3.994	46.76 \pm 7.89
S XVI	7.40	$2p \rightarrow 2P_{3/2} \rightarrow 1s$	4.727	4.731	77.71 \pm 9.85	4.732	3.34 \pm 3.02
S XV	7.20	$1s \rightarrow 2p \rightarrow 1s^2$	5.038	5.041	147.70 \pm 13.18	5.036	9.18 \pm 4.15
Si XIV	7.20	$2p \rightarrow 2P_{3/2} \rightarrow 1s$	6.180	6.184	409.75 \pm 21.26	6.185	20.85 \pm 5.64
Si XIII	7.00	$1s \rightarrow 2p \rightarrow 1s^2$	6.650	6.649	579.86 \pm 25.09	6.652	28.23 \pm 6.38
Si XIII	6.95	$1s \rightarrow 2p \rightarrow 1s^2$	6.688	6.688	52.49 \pm 8.29
Si XIII	7.00	$1s \rightarrow 2s \rightarrow 1s^2$	6.740	6.740	371.91 \pm 20.30	6.740	9.63 \pm 4.22
Mg XII	7.00	$3p \rightarrow 2P_{3/2} \rightarrow 1s$	7.110	7.109	191.56 \pm 14.86
Fe XXIV	7.30	$1s^2 \rightarrow 5p \rightarrow 2P_{3/2} \rightarrow 1s^2$	7.170	7.168	193.70 \pm 14.94
Mg XI	6.85	Unknown	7.473	7.471	132.60 \pm 12.54
Al XII	6.90	$1s \rightarrow 2p \rightarrow 1s^2$	7.760	7.757	166.77 \pm 13.94	7.757	6.88 \pm 3.71
Mg XI	6.80	$1s \rightarrow 3p \rightarrow 1s^2$	7.850	7.852	186.06 \pm 14.66
Fe XXIV	7.29	$1s^2 \rightarrow 4p \rightarrow 2P_{3/2} \rightarrow 1s^2$	7.985	7.986	211.71 \pm 15.57	7.980	13.53 \pm 4.77
Fe XXIII	7.20	$2s \rightarrow 4p \rightarrow 1s^2$	8.300	8.310	261.50 \pm 17.19
Mg XII	7.00	$2p \rightarrow 2P_{3/2} \rightarrow 1s$	8.419	8.420	1030.06 \pm 33.10	8.422	36.62 \pm 7.11
Fe XXIII	7.20	$2s \rightarrow 4d \rightarrow 1D_2 \rightarrow 2s$	8.810	8.812	196.60 \pm 15.04
Fe XXII	7.10	$2s^2 \rightarrow 4d \rightarrow 2D_{3/2} \rightarrow 2s^2$	8.980	8.973	149.39 \pm 13.25
Mg XI	6.81	$1s \rightarrow 2p \rightarrow 1s^2$	9.168	9.169	651.05 \pm 23.45	9.168	15.59 \pm 5.04
Mg XI	6.81	$1s \rightarrow 2p \rightarrow 1s^2$	9.231	9.234	162.23 \pm 13.76
Mg XI	6.81	$1s \rightarrow 2s \rightarrow 1s^2$	9.314	9.314	316.62 \pm 18.81	9.310	26.30 \pm 6.20
Fe XXI	7.10	$2s^2 \rightarrow 2p \rightarrow 4d \rightarrow 3D_1 \rightarrow 2s^2$	9.480	9.479	112.90 \pm 11.66
Fe XXI	7.10	Unknown	9.542	9.545	37.14 \pm 7.15
Ne X	6.81	$4p \rightarrow 2P_{3/2} \rightarrow 1s$	9.708	9.707	269.70 \pm 17.44
Ni XXV	7.30	$2s \rightarrow 3d \rightarrow 1D_2 \rightarrow 2s$	9.970	9.993	170.32 \pm 14.07
Na XI	6.90	$2p \rightarrow 2P_{1/2} \rightarrow 1s$	10.020	10.038	264.61 \pm 17.29
Ne X	6.78	$3p \rightarrow 2P_{3/2} \rightarrow 1s$	10.238	10.239	566.43 \pm 24.81	10.242	15.22 \pm 4.99
Fe XXV	7.75	Unknown	10.369	10.362	142.44 \pm 12.96
Fe XXIV	7.27	$1s^2 \rightarrow 3p \rightarrow 2P_{3/2} \rightarrow 1s^2$	10.619	10.625	287.08 \pm 17.96	10.616	11.42 \pm 4.48
Fe XXIV	7.27	$1s^2 \rightarrow 3p \rightarrow 2P_{1/2} \rightarrow 1s^2$	10.663	10.664	186.58 \pm 14.68	10.663	16.04 \pm 5.09
Ne IX	6.60	Unknown	10.764	10.768	120.82 \pm 12.02
Fe XXIII?	7.2	Unknown	10.825	10.817	114.83 \pm 11.75
Fe XXIII	7.20	$2s \rightarrow 3p \rightarrow 1P_1 \rightarrow 2s^2$	10.980	10.984	211.56 \pm 15.57	10.989	9.81 \pm 4.24
Fe XXIII	7.20	$2p \rightarrow 3p \rightarrow 3P_1 \rightarrow 2s^2$	11.020	11.028	265.94 \pm 17.33	11.028	15.75 \pm 5.06
Fe XXIV	7.29	$1s^2 \rightarrow 3d \rightarrow 2D_{5/2} \rightarrow 1s^2$	11.176	11.177	249.64 \pm 16.82	11.176	11.76 \pm 4.53
Fe XXIV	7.29	Unknown	11.260	11.259	139.02 \pm 12.69
Fe XVIII	6.90	Unknown	11.326	11.321	98.98 \pm 10.98
Fe XXIV	7.29	$1s^2 \rightarrow 3s \rightarrow 2S_{1/2} \rightarrow 1s^2$	11.432	11.430	302.00 \pm 18.39	11.430	10.97 \pm 4.42
Ne IX	6.60	$1s \rightarrow 3p \rightarrow 1P_1 \rightarrow 1s^2$	11.544	11.539	250.20 \pm 16.84
Fe XXIII	7.18	$2s \rightarrow 3d \rightarrow 1D_2 \rightarrow 2s$	11.736	11.741	298.14 \pm 18.28
Fe XXIII	7.10	$2s^2 \rightarrow 3d \rightarrow 2D_{3/2} \rightarrow 2s^2$	11.770	11.775	308.51 \pm 18.58	11.753	21.03 \pm 5.66
Fe XXII	7.10	$2s^2 \rightarrow 3d \rightarrow 2D_{5/2} \rightarrow 2s^2$	11.930	11.929	111.54 \pm 11.59	11.932	14.38 \pm 4.88
Fe XXI/XXII	7.1/7.1	Unknown	11.975	11.976	72.97 \pm 9.58
Ne X	6.77	$2p \rightarrow 2P_{3/2} \rightarrow 1s$	12.132	12.134	2099.93 \pm 46.83	12.134	53.21 \pm 8.34
Fe XXI	7.10	$2s^2 \rightarrow 2p \rightarrow 3d \rightarrow 3D_1 \rightarrow 2s^2$	12.284	12.284	470.20 \pm 22.70	12.282	20.38 \pm 5.59
Fe XXI	7.10	Unknown	12.397	12.398	108.70 \pm 11.46
Fe XXI	7.10	Unknown	12.649	12.650	135.44 \pm 12.67
Fe XX	7.00	Unknown	12.750	12.754	134.06 \pm 12.61
Fe XX	7.00	$2s^2 \rightarrow 2p^2 \rightarrow 3d \rightarrow 4P_{5/2} \rightarrow 2s^2$	12.827	12.827	451.24 \pm 22.26	12.840	17.36 \pm 5.25
Fe XX	7.00	Unknown	13.143	13.143	109.68 \pm 11.50
Ne IX	6.59	$1s \rightarrow 2p \rightarrow 1P_1 \rightarrow 1s^2$	13.447	13.449	503.49 \pm 26.53	13.453	13.63 \pm 4.79
Fe XXI	6.91	$2s \rightarrow 2p^2 \rightarrow 3s \rightarrow 3P_0 \rightarrow 2s$	13.518	13.515	354.99 \pm 19.86	13.551	9.25 \pm 4.16
Ne IX	6.59	$2p^3 \rightarrow 3d \rightarrow 3D_2 \rightarrow 2s^2$	13.553	13.554	109.67 \pm 11.50	13.701	22.28 \pm 5.79
Ne IX	6.59	$1s \rightarrow 2s \rightarrow 3S_1 \rightarrow 1s^2$	13.699	13.699	313.47 \pm 18.72
Fe XVIII	6.84	$2p^4 \rightarrow 3d \rightarrow 2D_{5/2} \rightarrow 2s^2$	14.208	14.206	404.66 \pm 21.13	14.204	17.64 \pm 5.28
Fe XVIII	6.84	$2p^4 \rightarrow 3d \rightarrow 2S_{1/2} \rightarrow 2s^2$	14.256	14.266	151.33 \pm 13.33	14.263	11.88 \pm 4.55
Fe XVIII	6.89	$2p^4 \rightarrow 3d \rightarrow 2D_{3/2} \rightarrow 2s^2$	14.373	14.372	238.64 \pm 16.47	14.382	16.81 \pm 5.19
Fe XVIII	6.90	$2p^4 \rightarrow 3d \rightarrow 2F_{5/2} \rightarrow 2s^2$	14.530	14.540	159.65 \pm 13.66
Fe XVIII	6.90	$2p^4 \rightarrow 3d \rightarrow 4P_{1/2} \rightarrow 2s^2$	14.580	14.585	48.67 \pm 8.03
Fe XIX	6.90	$2p^3 \rightarrow 3s \rightarrow 3D_3 \rightarrow 2s^2$	14.670	14.669	84.79 \pm 10.24
Fe XX	7.00	Unknown	14.754	14.755	63.24 \pm 8.99
Fe XX ?	7.00	Unknown	14.826	14.823	60.14 \pm 8.80
Fe XVII	6.72	$2p^5 \rightarrow 3d \rightarrow 1P_1 \rightarrow 2p^6$	15.014	15.014	653.29 \pm 26.57	15.013	45.75 \pm 7.81
Fe XIX	6.90	$2s \rightarrow 2p^4 \rightarrow 3s \rightarrow 3P_2 \rightarrow 2s$	15.080	15.081	121.42 \pm 12.05	15.083	6.21 \pm 3.63
O VIII	6.51	$4p \rightarrow 2P_{3/2} \rightarrow 1s$	15.176	15.175	135.37 \pm 12.66
Fe XVII	6.72	$2p^5 \rightarrow 3d \rightarrow 3D_1 \rightarrow 2p^6$	15.261	15.263	230.56 \pm 16.20	15.266	17.65 \pm 5.29
Fe XVII	6.70	$2p^5 \rightarrow 3d \rightarrow 3P_1 \rightarrow 2p^6$	15.450	15.457	79.499 \pm 9.95
Fe XX	7.10	$2p^4 \rightarrow (1D) \rightarrow 3s \rightarrow 2D_{5/2} \rightarrow 2s^2$	15.626	15.626	116.25 \pm 11.81
Fe XVIII	6.90	$2p^4 \rightarrow (3P) \rightarrow 3s \rightarrow 4P_{3/2} \rightarrow 2s^2$	15.828	15.823	76.51 \pm 9.79
Fe XVIII	6.90	$2p^4 \rightarrow (1P) \rightarrow 3s \rightarrow 2D_{3/2} \rightarrow 2s^2$	15.870	15.869	78.39 \pm 9.89
O VIII	6.50	$3p \rightarrow 2P_{3/2} \rightarrow 1s$	16.005	16.007	387.09 \pm 20.69	16.009	17.56 \pm 5.27
Fe XVIII	6.84	$2p^4 \rightarrow 3s \rightarrow 4P_{5/2} \rightarrow 2s^2$	16.071	16.073	229.54 \pm 16.17	16.076	7.37 \pm 3.85
Fe XIX	6.90	$2p^3 \rightarrow 3p \rightarrow 3P_2 \rightarrow 2s$	16.120	16.108	72.81 \pm 9.57
Fe XVIII	6.70	$2s \rightarrow 2p^5 \rightarrow 3s \rightarrow 2P_{3/2} \rightarrow 2s$	16.170	16.167	58.14 \pm 8.67
Fe XVII	6.71	$2p^5 \rightarrow 3s \rightarrow 3P_1 \rightarrow 2p^6$	16.780	16.776	208.22 \pm 18.57	16.773	12.55 \pm 4.64
Fe XVII	6.71	$2p^5 \rightarrow 3s \rightarrow 1P_1 \rightarrow 2p^6$	17.051	17.052	367.09 \pm 20.17	17.092	24.80 \pm 6.05
Fe XVII	6.71	$2p^5 \rightarrow 3s \rightarrow 3P_2 \rightarrow 2p^6$	17.096	17.096	306.81 \pm 18.53
O VIII	6.48	$2p \rightarrow 2P_{3/2} \rightarrow 1s$	18.967	18.970	781.22 \pm 28.96	18.970	27.80 \pm 6.34
O VII	6.33	$1s \rightarrow 2p \rightarrow 1P_1 \rightarrow 1s^2$	21.600	21.601	70.80 \pm 9.45
O VII	6.33	$1s \rightarrow 2p \rightarrow 1P_1 \rightarrow 1s^2$	21.800	21.804	27.55 \pm 6.32
O VII	6.33	$1s \rightarrow 2p \rightarrow 1P_1 \rightarrow 1s^2$	22.100	22.106	31.15 \pm 6.64	22.100	4.49 \pm 3.29
N VII	6.32	$2p \rightarrow 2P_{3/2} \rightarrow 1s$	24.779	24.780	57.54 \pm 8.63